KSME

Springer

Journal of Mechanical Science and Technology 36 (4) 2022

Original Article
DOI 10.1007/s12206-022-0306-4

Keywords:
· Threshold denoising
· Arctangent threshold function
· Empirical wavelet transform
· Rolling element bearing
· Fault feature extraction

Correspondence to:
Feiyun Xu
fyxu@seu.edu.cn

Citation:
Li, C., Xu, F., Yang, H., Zou, L. (2022). A rolling element bearing fault feature extraction method based on the EWT and an arctangent threshold function. Journal of Mechanical Science and Technology 36 (4) (2022) 1693~1708.
http://doi.org/10.1007/s12206-022-0306-4

Received August 9th, 2021
Revised December 22nd, 2021
Accepted December 27th, 2021

† Recommended by Editor
No-cheol Park

A rolling element bearing fault feature extraction method based on the EWT and an arctangent threshold function

Chao Li, Feiyun Xu, Hongxin Yang and Lei Zou

School of Mechanical Engineering, Southeast University, Nanjing 211189, China

Abstract Hard and soft threshold functions are discontinuous at the threshold and deviate at the wavelet estimation coefficient, respectively. Aiming at this problem, a rolling element bearing (REB) fault feature extraction method is proposed based on the empirical wavelet transform (EWT) and an arctangent threshold function (ATF). First, the input signal is decomposed with the EWT, and intrinsic mode functions (IMFs) containing fault information are selected according to their cross-correlation coefficients and kurtosis values. Second, the selected IMFs are denoised by the ATF. Finally, to extract the fault characteristic frequency and determine the fault type, the denoised IMFs are added to form a reconstructed signal for envelope analysis. The superiority of the proposed method is verified on simulation signals and actual fault signals (including two cases); the developed approach has strong denoising and fault feature extraction effects.

1. Introduction

Rolling element bearings (REBs), as critical parts of rotating machinery, are becoming increasingly significant in applications [1-3], such as wind turbines [4], aero-engines [5] and driving motors [6]. The condition of bearings largely determines the safety statuses of mechanical systems. Bearing fault vibration signals are usually nonlinear and nonstationary signals. Due to the error of measuring equipment and the interference of external factors, signals become mixed with noise in actual vibration signal measurements. This induces adverse effects on subsequent signal processing and fault diagnosis steps.

To accurately obtain signals, the collected signals are usually denoised before conducting signal processing, and the most commonly used denoising method is the threshold denoising method. Donoho [7, 8] proposed two threshold functions: a hard threshold function (HTF) and a soft threshold function (STF). Both functions are applied frequently, but they have shortcomings. The discontinuity of the HTF leads to local oscillations in the reconstructed signal after denoising. The reconstructed signal becomes distorted due to the continuous deviation of the STF. Meng et al. [9] proposed an improved wavelet threshold function and implemented it for REB fault feature extraction. By adjusting specific parameters, the function could realize “hard” or “soft” characteristics, and it effectively removed noise. However, the specific parameters in this method had unclear physical meanings and lacked a theoretical basis. A new threshold function supporting a different wavelet threshold calculation strategy was proposed in Ref. [10]. The strategy reduced the deviations of inaccurate thresholds by studying their wavelet decomposition layers. In addition, the new threshold function eliminated the constant deviation and resolved the discontinuity problem, but its denoising effect was not ideal in cases with strong noise. Li et al. [11] presented an approach for downhole microseismic signals based on an improved threshold function (ITF) and the empirical wavelet transform (EWT). This approach fused its designed threshold function and the traditional HTF. It had good performance in terms of improving the signal-to-noise ratio (SNR) and preserving detailed information. Chegini et al. [12] used the ITF developed in Ref. [11] and applied it to REB fault diagnosis. In addition,

the ITF was more sensitive to kurtosis than the STF. Chen et al. [13] combined wavelet threshold denoising, energy entropy and the particle swarm optimization-based least-squares support vector machine algorithm (PSO-LSSVM), and the effectiveness of this strategy was verified through fault diagnosis experiments with REBs. He et al. [14] set thresholds at different scales according to the standard noise deviation of the input and proposed an ITF based on the hierarchical threshold, which achieved an improved denoising effect for seismic signals. Chen et al. [15] improved the dual-threshold method of heart sound signal localization and segmentation by adding an additional heart sound rejection function and realized the localization and segmentation of heart sound signals with noise. A layered adaptive threshold function was proposed in Ref. [16]; this function was continuous and differentiable at the threshold. Although this method overcame the shortcomings of traditional threshold denoising, it needed to calculate the trend parameter and threshold repeatedly, which increased its computational cost. Liu et al. [17] used Gaussian mixture models and criteria to evaluate noise variance. They designed an enhanced wavelet threshold function with thresholds at various scales, which had reliable performance in terms of denoising and retaining original signal characteristics. Bayer et al. [18] proposed an iterative wavelet threshold called "*SpcShrink*" for signal denoising. Through discussions of two empirical applications in real biomedical data filtering, *SpcShrink* exhibited superior performance when compared with *VisuShrink* [19], *SureShrink* [8], *BayesShrink* [20] and *S-median* [21].

Given the shortcomings and deficiencies of traditional threshold functions, the arctangent threshold function (ATF) is proposed. It has a "soft" continuous property. Additionally, it has characteristics like "hard" and avoids constant deviation. Based on the EWT, cross-correlation coefficient, kurtosis, envelope analysis and ATF, an REB fault feature extraction method is proposed.

The content is arranged as follows. Sec. 2 gives a brief overview of the EWT algorithm and analyzes the characteristics of traditional hard and soft threshold functions. Then, the ATF is established. Sec. 3 introduces the proposed method and its steps. In Sec. 4, simulated signals are processed using the proposed method. Additionally, the faulty signals of actual bearings are analyzed in Sec. 5, which includes two cases. The results are compared with those of other methods. In Sec. 6, the proposed method is discussed. The conclusions are drawn in Sec. 7.

2. Theory

2.1 Empirical wavelet transform

In 2013, French scholar Gilles [22] proposed a data-driven adaptive decomposition algorithm called the EWT. First, the algorithm segments the input signal spectrum and constructs a set of adaptive wavelet filter banks; then, it analyzes different frequency components to extract modulation signals with tight support characteristics.

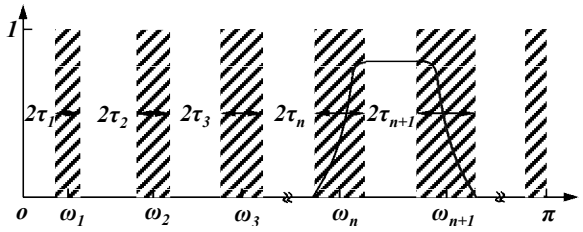

Fig. 1. Frequency band partition.

The construction of the wavelet filter bank is comparable to constructing a series of bandpass filters. Because every intrinsic mode function (IMF) surrounds a certain frequency, the normalized frequency spectrum of a raw signal can be divided into *N* frequency bands according to IMFs containing different frequencies (Fig. 1). The boundary between each frequency band is denoted by ω_n, and each ω_n considers a transition stage T_n with a width of $2\tau_n$.

Gilles adopted the idea regarding the construction of Meyer and Littlewood Paley wavelets to design a filter bank. The empirical scale function $\hat{\phi}_n(\omega)$ and empirical wavelet function $\hat{\psi}_n(\omega)$ are expressed by Eqs. (1) and (2), respectively:

$$\hat{\phi}_n(\omega)=\begin{cases}1, & |\omega|\le\omega_n-\tau_n\\ \cos\left[\frac{\pi}{2}\beta\left(\frac{1}{2\tau_n}\left(|\omega|-\omega_n+\tau_n\right)\right)\right], & \omega_n-\tau_n\le|\omega|\le\omega_n+\tau_n\\ 0, & otherwise\end{cases}, \tag{1}$$

$$\hat{\psi}_n(\omega)=\begin{cases}1, & \omega_n+\tau_n\le|\omega|\le\omega_{n+1}-\tau_{n+1}\\ \cos\left[\frac{\pi}{2}\beta\left(\frac{1}{2\tau_n}\left(|\omega|-\omega_{n+1}+\tau_{n+1}\right)\right)\right], & \omega_{n+1}-\tau_{n+1}\le|\omega|\le\omega_{n+1}+\tau_{n+1}\\ \sin\left[\frac{\pi}{2}\beta\left(\frac{1}{2\tau_n}\left(|\omega|-\omega_n+\tau_n\right)\right)\right], & \omega_n-\tau_n\le|\omega|\le\omega_n+\tau_n\\ 0, & otherwise\end{cases} \tag{2}$$

where the function $\beta(x)$ can be expressed by Eq. (3), τ_n is calculated by Eq. (4), and γ satisfies Eq. (5):

$$\beta(x)=\begin{cases}0, & x\le 0\\ \nu(x), & 0\le x\le 1\\ 0, & x\ge 1\end{cases}, \tag{3}$$

$$\tau_n=\gamma\omega_n, \tag{4}$$

$$0<\gamma<1 \text{ and } \gamma<\min_n\left(\frac{\Omega_{n+1}-\Omega_n}{\Omega_{n+1}+\Omega_n}\right) \tag{5}$$

where $\nu(x)$ in Eq. (3) is as follows:

$$v(x)=x^4\left(35-84x+70x^2-20x^3\right). \tag{6}$$

The detailed coefficients of the empirical wavelet are the inner product of the raw signal with $\hat{\psi}_n(\omega)$, and the approximate coefficients are the inner product of the raw signal with $\hat{\phi}_n(\omega)$. They are expressed as Eqs. (7) and (8), respectively:

$$\begin{aligned} W_f^{\varepsilon}(n,t)&=\langle f,\psi_n\rangle=\int f(\tau)\overline{\psi_n}(\tau-t)d\tau \\ &=F^{-1}\left(\hat{f}(\omega)\overline{\hat{\psi}_n}(\omega)\right), \end{aligned} \tag{7}$$

$$\begin{aligned} W_f^{\varepsilon}(0,t)&=\langle f,\phi_1\rangle=\int f(\tau)\overline{\phi_1}(\tau-t)d\tau \\ &=F^{-1}\left(\hat{f}(\omega)\overline{\hat{\phi}_1}(\omega)\right). \end{aligned} \tag{8}$$

According to the above deduction, the input raw signal can be expressed by Eq. (9).

$$\begin{aligned} f(t)&=W_f^{\varepsilon}(0,t)*\phi_1(t)+\sum_{n=1}^{N}W_f^{\varepsilon}(n,t)*\psi_n(t) \\ &=F^{-1}\left(W_f^{\varepsilon}(0,\omega)*\hat{\phi}_1(\omega)+\sum_{n=1}^{N}W_f^{\varepsilon}(n,\omega)*\hat{\psi}_n(\omega)\right) \end{aligned} \tag{9}$$

where the Fourier transformations of $W_f^{\varepsilon}(0,t)$ and $W_f^{\varepsilon}(n,t)$ are $W_f^{\varepsilon}(0,\omega)$ and $W_f^{\varepsilon}(n,\omega)$, respectively. Therefore, the raw signal $f(t)$ can be obtained via the combination of $p_k(t)$.

$$\begin{cases} p_0(t)=W_f^{\varepsilon}(0,t)*\phi_1(t) \\ p_1(t)=W_f^{\varepsilon}(1,t)*\psi_1(t) \\ \quad\vdots \\ p_k(t)=W_f^{\varepsilon}(n,t)*\psi_k(t) \end{cases} \tag{10}$$

where $p_k(t)$ is the independent component of the raw signal. Additionally, $f(t)$ is described by Eq. (11):

$$f(t)=\sum_{k=0}^{N}p_k(t). \tag{11}$$

The EWT features empirical mode decomposition (EMD) [23] and a wavelet transform (WT), which theoretically contribute to eliminating the end effect and mode aliasing. Compared with the EMD method, the EWT has a lower computational complexity and faster speed in processing vibration signals [12], so the EWT can be used as a powerful tool for REB fault feature extraction.

2.2 Analysis of the hard and soft threshold functions

Eqs. (12) and (13) are the expressions of the hard and soft threshold functions, respectively [7, 8]:

$$\tilde{c}_i(t)=\begin{cases} c_i(t), & |c_i(t)|\geq\lambda_i \\ 0, & |c_i(t)|<\lambda_i \end{cases}, \tag{12}$$

$$\tilde{c}_i(t)=\begin{cases} sign\left(c_i(t)\right)\left[|c_i(t)|-\lambda_i\right], & |c_i(t)|\geq\lambda_i \\ 0, & |c_i(t)|<\lambda_i \end{cases} \tag{13}$$

where i and t are positive integers (i from 1 to M; t from 1 to N), $c_i(t)$ is the component obtained after decomposition, $\tilde{c}_i(t)$ is the denoised version of $c_i(t)$, λ_i is the threshold corresponding to $c_i(t)$, and $sign(\cdot)$ is the sign function. The fixed threshold from Ref. [7] is used in this paper, and the threshold λ_i is calculated by Eq. (14):

$$\lambda_i=b\sigma_i\sqrt{2\ln N_s} \tag{14}$$

where N_s represents the total number of sampling points, b is set based on experience (here, it is set to 0.15), σ_i represents the standard deviation of the noise contained in the i-th component, and σ_i is usually calculated by using Eq. (15) from [7]:

$$\sigma_i=\sqrt{\frac{median\left(\left|c_i(t)\right|\right)}{0.6745}} \tag{15}$$

where $median(\cdot)$ represents the median function.

The hard and soft threshold functions are presented in Fig. 2, and three points can be deduced.

1) Both of these functions are odd, and their values remain zero in the interval $(-\lambda,\lambda)$.

2) The STF is continuous throughout the definition domain, whereas the HTF is discontinuous at the threshold.

3) When $|c_i|\geq\lambda$, the slopes of these two threshold functions are both 1, and there is a constant deviation between them. The deviation in the first quadrant is λ, and that in the third quadrant is $-\lambda$.

For point 1, the odd function characteristics of the threshold function are illustrated; thus, analyzing the first quadrant in the subsequent analysis satisfies its demands. For point 2, the discontinuity in the threshold makes the subsequent processing results oscillate more than those of the continuous threshold function. Point 3 shows that the STF always features a constant deviation in terms of denoising, which negatively impacts on the accuracy of the denoised signal.

2.3 Arctangent threshold function

To overcome the shortcomings mentioned in Sec. 2.2, the ATF is proposed here. In addition, it is constructed by scaling, rotating, and translating the coordinate system. Simultaneously, it is a natural function with two parallel asymptotes. When it is near the threshold, it has a continuous characteristic that is "soft"; when it is much larger than the threshold, it can prevent the constant deviation of the soft threshold and has a "hard"

characteristic.

The arctangent function can be expressed by Eq. (16):

$$y = \arctan(x) . \tag{16}$$

The first step is scaling, which is performed as follows:

$$y = \frac{\lambda_i}{\pi\sqrt{2}} \arctan(x) \tag{17}$$

where λ_i represents the threshold of the *i*-th IMF.

The second step is rotation, and the coordinate system rotation formula is as follows:

$$\begin{cases} x' = x\cos\theta - y\sin\theta \\ y' = x\sin\theta + y\cos\theta \end{cases} \tag{18}$$

where x and y are the abscissa and ordinate before rotation, respectively, x' and y' are the abscissa and ordinate after rotation, and θ is the rotation angle (counterclockwise rotation is positive; clockwise rotation is negative).

The slopes of the hard and soft threshold functions are both one (here, θ is 45°). Substituting the arctangent function into Eq. (18), Eq. (19) is obtained:

$$\begin{cases} x' = \dfrac{\sqrt{2}}{2}\left(x - \dfrac{\lambda_i \arctan x}{\pi\sqrt{2}}\right) \\ y' = \dfrac{\sqrt{2}}{2}\left(x + \dfrac{\lambda_i \arctan x}{\pi\sqrt{2}}\right) \end{cases} . \tag{19}$$

The third step is translation. Eq. (19) is moved between the two threshold functions. Then, the translation result is shown in Eq. (20):

$$\begin{cases} x' = \dfrac{\sqrt{2}}{2}\left(x - \dfrac{\lambda_i \arctan x}{\pi\sqrt{2}}\right) + q \\ y' = \dfrac{\sqrt{2}}{2}\left(x + \dfrac{\lambda_i \arctan x}{\pi\sqrt{2}}\right) + q - \dfrac{1}{2}\lambda_i \end{cases} . \tag{20}$$

Finally, the ATF is shown in Eq. (21):

$$\tilde{c}_i(t) = \begin{cases} \dfrac{\sqrt{2}}{2}\left(x + \dfrac{\lambda_i \arctan x}{\pi\sqrt{2}}\right) + q - \dfrac{1}{2}\lambda_i, & |c_i(t)| \geq \lambda_i \\ 0, & |c_i(t)| < \lambda_i \end{cases} \tag{21}$$

$$where \ \ c_i(t) = \frac{\sqrt{2}}{2}\left(x - \frac{\lambda_i \arctan x}{\pi\sqrt{2}}\right) + q .$$

q is the position parameter. When *q* is much greater than zero, the ATF is "soft"; when *q* is close to zero, the ATF behaves as a "hard" feature. Notably, the ATF is an implicit function. First, x is solved by the known $c_i(t)$, and then Eq. (21) is substituted to calculate $\tilde{c}_i(t)$. Generally, this value can be calculated by numerical methods.

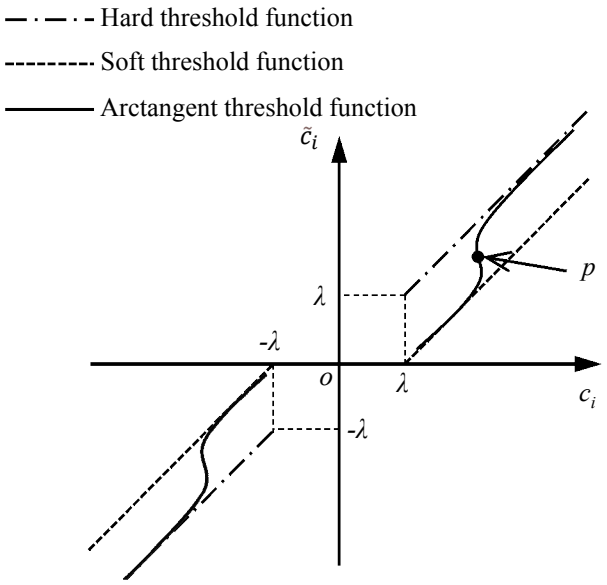

Fig. 2. Three kinds of threshold functions.

The ATF is shown in Fig. 2, where the coordinates of *p* are defined as $(q, q - 0.5\times\lambda_i)$. In the research, results have shown that the position parameter *q* is mainly determined by the proportion of noise components contained in the raw signal. Moreover, the size of the position parameter *q* directly affects whether the ATF is "hard" or "soft", thereby affecting the denoising and fault feature extraction performance of the function. In practice, the magnitude of the position parameter *q* can be adjusted according to the feedback obtained via the experimental results. The value range of the position parameter *q* is recommended to be $10\lambda_i$ - $60\lambda_i$.

3. The proposed method

On the basis of the ATF proposed in Sec. 2.3, an REB fault feature extraction method utilizing the EWT, cross-correlation coefficient, kurtosis and envelope analysis is proposed. The flowchart is shown in Fig. 3.

Steps:

1) The raw signal is decomposed using the EWT to obtain IMFs (the total is *M*, and the initial value of *m* is set to 1).

2) Calculate the cross-correlation coefficient between the *m*-th IMF and the raw signal according to Eq. (22). In addition, calculate the kurtosis of the *m*-th IMF according to Eq. (23).

$$\rho_{sm} = \left| \frac{\sum_{n=1}^{N}\left[c_m(n) - \overline{c_m}\right]\left[s(n) - \overline{s}\right]}{\sqrt{\sum_{n=1}^{N}\left[c_m(n) - \overline{c_m}\right]^2}\sqrt{\sum_{n=1}^{N}\left[s(n) - \overline{s}\right]^2}} \right| \tag{22}$$

where c_m represents the *m*-th IMF and s is the raw signal.

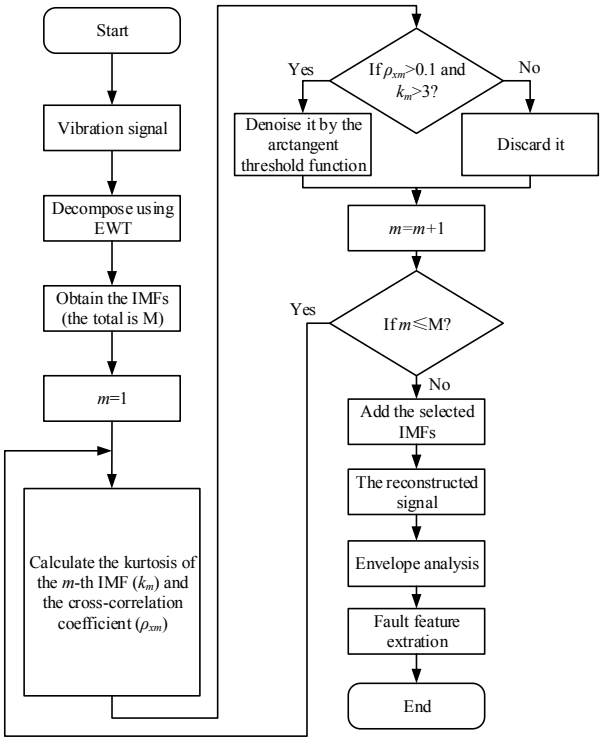

Fig. 3. Flow chart of the proposed method.

$\overline{c}_m$ and $\overline{s}$ are the mean values of c_m and s, respectively. ρ_{sm} is the cross-correlation coefficient between s and c_m.

$$k_m = \frac{E(s-\mu)^4}{\sigma^4} \tag{23}$$

where k_m represents the kurtosis of the m-th IMF, μ represents the mean value, $E(\bullet)$ represents the expectation, and σ represents the standard deviation.

3) Determine whether the m-th IMF satisfies $\rho_{sm} > \rho$ and $k_m > k$. If yes, go to the next step; otherwise discard the m-th IMF (where ρ and k are set to 0.1 and 3, respectively, based on experience [12]). In addition, set $m = m + 1$.

4) According to Eqs. (14) and (15), calculate the threshold of the selected IMF and use the ATF to denoise it.

5) Repeat steps 2-4 until m>M.

6) After denoising the selected IMFs, add them to obtain a reconstructed signal.

7) Extract fault characteristic frequency through envelope analysis, and then identify the fault type.

4. Analysis of simulation signals

4.1 Simulation signal model

The bearing simulation signals are generated according to an outer race fault vibration signal model of the bearing [24, 25]:

Table 1. Parameters of the bearing outer race fault vibration signal model.

Parameter	N	A	T_d	B	ξ	φ_n	f_n
Value	110	1	1/110	0.25	900	0	3000

$$x_{OR}(t) = f(t) * h(t) + n(t), \tag{24}$$

$$f(t) = \sum_{k=0}^{N-1} A_k \delta\left(t - kT_d \pm R(r, T_d)\right), \tag{25}$$

$$n(t) = Noise(0, -12) \tag{26}$$

where * represents convolution, $f(t)$ represents the cyclic impact signal, $\delta(t)$ represents the unit pulse function, $n(t)$ represents Gaussian white noise with a -12 dB SNR (the setting of the SNR is discussed in Sec. 6.1), T_d represents the period interval between two adjacent pulses, N represents the total number of impact pulses, A_k represents the intensity of the impact signal, and $R(r, T_d) = rT_d$ represents the time deviation of the k-th pulse repetition cycle (which is approximately 1 %-2 % of T_d, and the slip rate r is set to 1.5 % in this paper). The impulse response signal $h(t)$ caused by a bearing fault is expressed as Eq. (27):

$$h(t) = Be^{-\xi t}\cos(2\pi f_n t + \varphi_n) \tag{27}$$

where B is the intensity of the impulse response signal, φ_n is the initial phase, ξ is the attenuation coefficient, and f_n represents the natural frequency of the excitation system. Moreover, the sampling frequency is 10240 Hz, and the total sampling time is 1 second, so the total number of points is 10240. The specific parameters of the bearing outer race fault vibration signal model are presented in Table 1.

4.2 Fault feature extraction from simulation signals

For the clarity of the discussion and statements, the following four threshold functions are denoted as {no threshold function = NTF; soft threshold function = STF; hard threshold function = HTF; improved threshold function in Ref. [11]= ITF; arctangent threshold function = ATF}. Fig. 4 shows the time-domain waveform, frequency spectrum and envelope spectrum of the raw signal. Fig. 5(a) shows the time-domain waveform, frequency spectrum and envelope spectrum of the noisy signal. Noise is distributed in the frequency spectrum, so it is difficult to distinguish the fault character frequency from the envelope spectrum. Fig. 6 presents a series of time-domain waveforms for each IMF. The 10th, 13th, and 14th IMFs are selected by referring to the cross-correlation coefficient and kurtosis criterion, and then they are denoised by the ATF and combined as a reconstructed signal. Eventually, the signal is processed by envelope analysis to obtain the envelope spectrum.

Fig. 5(b) shows the time-domain waveform, spectrum and envelope spectrum of the signal processed without EWT decomposition. If the signal is directly denoised by the ATF with-

out EWT decomposition, the corresponding fault characteristic frequency cannot be determined. As shown in Fig. 5(c), the frequency spectrum indicates that the process of selecting IMFs is similar to filtering the signal by using multiple sets of bandpass filters. Fig. 5(d) shows the detailed processing results of the signal after it is denoised by the ATF. From Figs. 5(c) and (d), the fault characteristic frequency is clearly distinguished (f_{so} = 110 Hz) in the envelope spectra. Furthermore, comparing these spectra with those in Fig. 5(a), it is found that the harmonics and noise are effectively eliminated. However, the harmonic frequency in Fig. 5(d) is more evident than that in Fig. 5(c), which demonstrates that using the ATF for denoising improves the accuracy of recognizing the fault characteristic frequency and its harmonics.

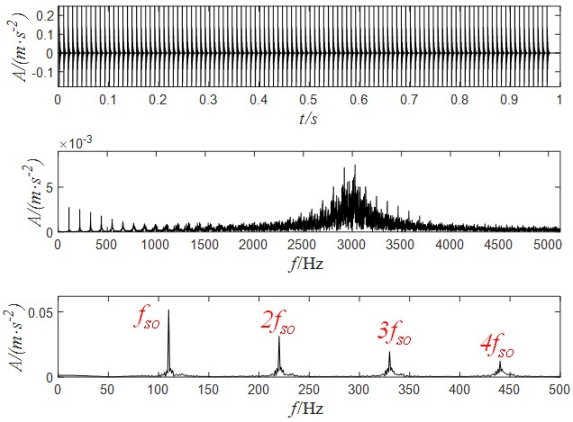

Fig. 4. Time-domain waveform, spectrum and envelope spectrum of the raw signal.

To verify the superiority of the ATF in terms of denoising the noisy signal, the NTF, HTF, STF, ITF, and ATF are compared on four indicators: kurtosis, the SNR, the cross-correlation coefficient (XCORR) and the mean square error (MSE). Their calculation formulas are shown in Eqs. (23), (28)-(30), respectively.

$$SNR = 10 \times \log_{10}\left(\frac{P_S}{P_N}\right), \tag{28}$$

$$XCORR = \frac{E\left[\left(s_{noise} - \overline{s}_{noise}\right)\left(x - \overline{x}\right)\right]}{\sigma_{s_{noise}}\sigma_x}, \tag{29}$$

$$MSE = \frac{1}{N}\sum_{n=1}^{N}\left[s_{noise}(n) - x(n)\right]^2 \tag{30}$$

where P_S represents the effective power of the raw signal, and P_N represents the effective power of the noise. x represents the denoised signal and s_{noise} is the noisy signal. $\overline{x}$ and $\overline{s}_{noise}$ are the mean values of x and $\overline{s}_{noise}$, respectively, $E(\bullet)$

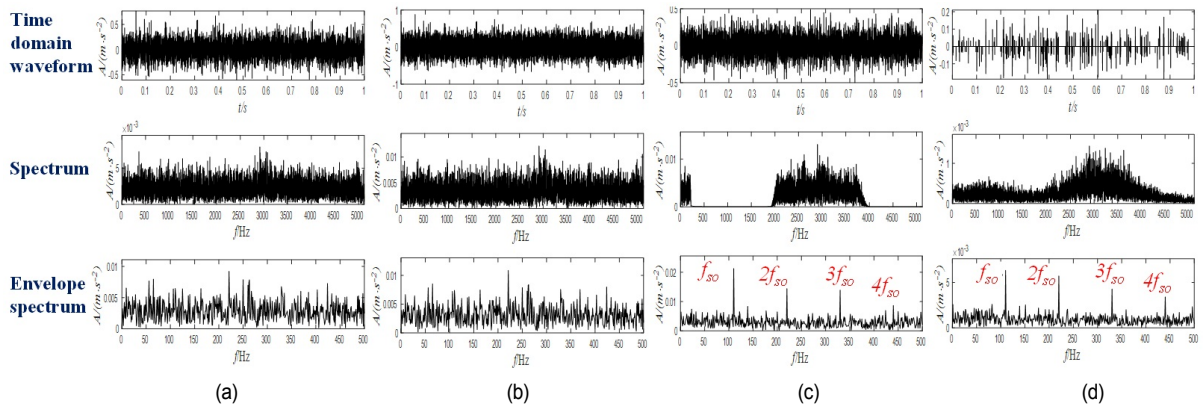

Fig. 5. Time-domain waveforms, spectra and envelope spectra: (a) noisy signal; (b) without EWT decomposition; (c) denoised by the NTF; (d) denoised by the ATF.

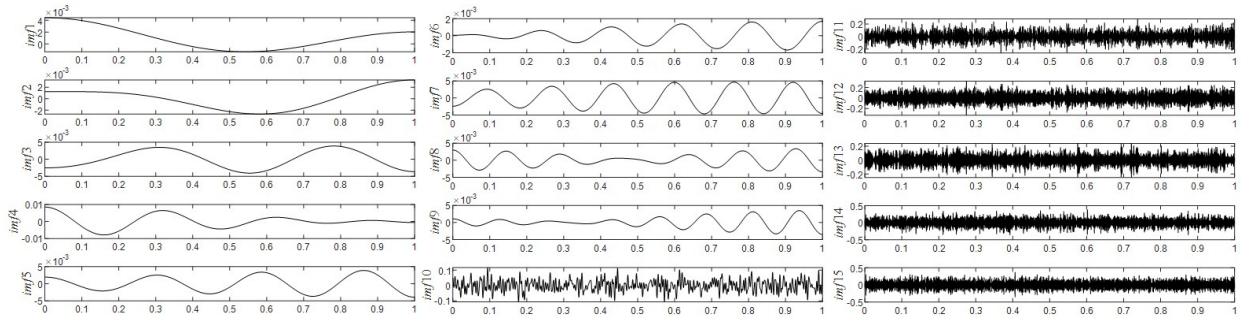

Fig. 6. Time-domain waveforms of the IMFs decomposed by the EWT.

Table 2. Comparison of the evaluation indices produced by different methods in the simulation signal analysis.

Method	Kurtosis	SNR	XCORR	MSE
The noisy signal	3.0167	-11.9350	1	0
Without EWT	12.7290	-1.6441	0.6381	0.02355
No threshold function	3.2201	-7.3020	0.6033	0.02370
Hard threshold function	23.7270	-1.8398	0.2760	0.03442
Soft threshold function	72.8430	0.2917	0.2330	0.03640
Improved threshold function [11]	77.4240	0.2901	0.2312	0.03638
Arctangent threshold function	45.9240	0.3550	0.2608	0.03594

represents the expectation, and σ represents the standard deviation.

The values of the four indicators achieved by the different methods are shown in Table 2. The verification process includes two parts: verification of the proposed method and verification of ATF.

First, the proposed method mainly considers three aspects (whether to use the EWT, whether to use the threshold function for denoising, and which threshold function to use). In addition, the total comparison includes four groups: the first is the noisy signal group that directly performs envelope analysis on the input signal; the second is the "without EWT" group that denoises the noisy signal via the ATF without EWT decomposition and then processes it by envelope analysis; the third is the "no threshold function" group that does not denoise the IMFs decomposed by the EWT with any threshold function and then adds these IMFs as the reconstructed signal for envelope analysis; the last group is threshold function group that denoises the IMFs decomposed by the EWT with different threshold functions and then adds the result as the reconstructed signal for envelope analysis. The threshold function group includes the HTF, STF, ITF and ATF.

Fig. 5 and Table 2 show that the noisy signal group and "without EWT" group fail to extract the fault characteristic frequency from the envelope spectrum. The signal itself contains excessive noise, which increases the difficulty of threshold denoising without EWT decomposition. Therefore, it is not feasible to directly perform envelope analysis on the signal under strong noise. Moreover, the kurtosis and SNR of the noisy signal group are inferior to those of the "no threshold function" group and the threshold function group. Both the "no threshold function" group and the threshold function group can extract the fault characteristic frequency and its harmonics. However, the recognition accuracy of the "no threshold function" group is lower than that of the threshold function group. Although the "no threshold function" group performs slightly more reliably than the threshold function group in terms of the XCORR and the MSE, the threshold function group achieves better performance in terms of kurtosis and the SNR. Relative to those of the noisy signal group and the "no threshold function" group, the kurtosis and SNR of the threshold function group are significantly improved.

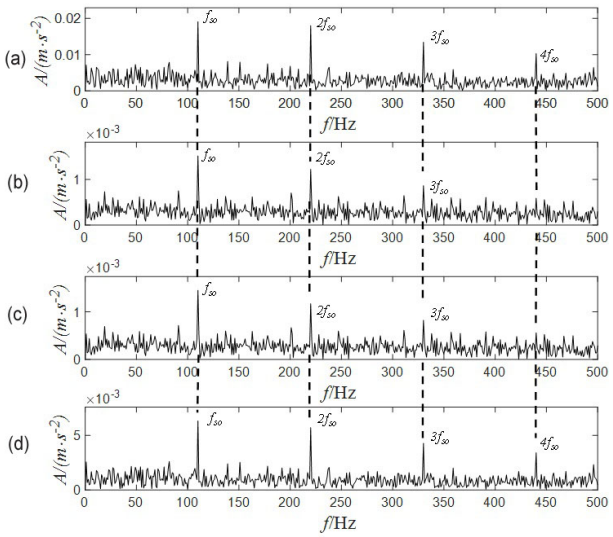

Fig. 7. The envelope spectra of the signal processed with four threshold functions: (a) HTF; (b) STF; (c) ITF; (d) ATF.

Second, the superiority of the ATF is verified. It can be concluded from Table 2 that for kurtosis, the ITF, STF and ATF yield significant increases in the kurtosis, and their values are much larger than those of the HTF. An essential and effective indicator to measure the performance of denoising is the SNR. In the threshold function group, it is evident that the ATF has the largest SNR, so its denoising effect is better than that of the other three threshold functions. Moreover, its XCORR is the second largest, and its MSE is the second smallest. The XCORR is an index used to measure the degree of correlation between two different time series. The larger the XCORR is, the more similar the two different time series; the smaller the MSE is, the higher the denoising efficiency [26]. Then, the identification accuracies achieved for the fault frequency and its harmonics are compared. The fault characteristic frequency can be clearly distinguished from the envelope spectra denoised by the four different threshold functions (Fig. 7). In the envelope spectra of the signal after denoising with both the ATF and HTF, the distinguishable maximum frequency is a 4x frequency component. In contrast, the 4x frequency components in the envelope spectra of the signal denoised by both the STF and ITF are not prominent. The STF and ITF are worse than the HTF and ATF in terms of the recognition accuracy for the fault frequency and its harmonics. From the preceding analysis, it is convincing that the ATF is superior to the HTF, STF and ITF.

In summary, the proposed method can enhance the recognition accuracy of the fault characteristic frequency and its harmonics. In the next section, the validity of the proposed method is verified through an actual bearing fault signal.

5. Analysis of actual bearing fault signals

5.1 Case 1: experimental data obtained from a laboratory

5.1.1 Bearing fault signal acquisition

The vibration signals of HRB6205 REBs are collected as actual bearing fault signals. The ABLT-1A experimental bench is composed of loads, a drive system, electrical controllers, bearing signal acquisition modules and a condition monitoring device (Fig. 8). The acceleration sensor is fixed directly above the faulty bearing. Inner and outer race faults are artificially manufactured on the HRB6205 REBs by electrodischarge during the experiment. The faulty defect size is 1.6 mm (width)×2 mm (depth) for the outer race and 1.6 mm (width)×4 mm (depth) for the inner race. The specific characteristics of the HRB6205 REBs are listed in Table 3. During the experiment, the rotation speed is 1050 r/min, the load is 0 kg, the sampling frequency is 10240 Hz, and the sampling time is 1 second.

Table 3. Geometric parameters of HRB6205 bearings.

Parameter	Pitch diameter	Ball diameter	Rolling elements	Contact angle
Value	39.04 mm	7.94 mm	9	0°

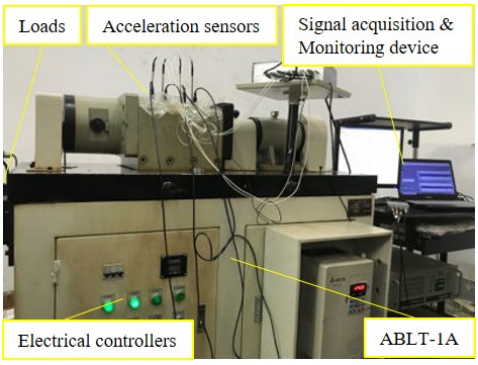

Fig. 8. The experimental bench.

Eqs. (31) and (32) calculate the theoretical characteristic frequencies of the bearing outer race faults and inner race faults, respectively [27]:

$$BPFO = \frac{n_b}{2} F_r \left(1 - \frac{d}{D}\cos\alpha\right), \tag{31}$$

$$BPFI = \frac{n_b}{2} F_r \left(1 + \frac{d}{D}\cos\alpha\right) \tag{32}$$

where n_b is the number of rolling elements, F_r is the rotation speed, d is the diameter of the rolling elements, D is the pitch diameter, and α is the contact angle. Through calculation, the outer ring fault frequency f_o is approximately 62 Hz, and the inner ring fault frequency f_i is approximately 95 Hz.

5.1.2 Outer race fault feature extraction for REBs

From Fig. 9(a), noise is distributed in the whole frequency domain, and the low-frequency harmonic component is large. Therefore, there is a considerable obstacle to accurately determining the fault characteristic frequency from the envelope spectrum. Fig. 10 shows the IMFs obtained after EWT decomposition. The 13th, 14th and 15th IMFs are selected according to the kurtosis and cross-correlation criteria, and the reconstructed signal is obtained after denoising with the ATF. Finally, the reconstructed signal is analyzed via envelope analysis.

Fig. 9(b) shows the time-domain waveform, spectrum and envelope spectrum of the signal produced without EWT decomposition. The result is the same as that in Sec. 4.2; it is difficult to extract the fault characteristic frequency without EWT decomposition. Fig. 9(c) shows the time-domain waveform, spectrum and envelope spectrum of the reconstructed signal produced with NTF denoising. Fig. 9(d) shows the time-domain waveform, spectrum and envelope spectrum of the reconstructed signal produced with ATF denoising. From the frequency spectrum of Fig. 9(c), it can be concluded that the selection process has the function of low-frequency filtering.

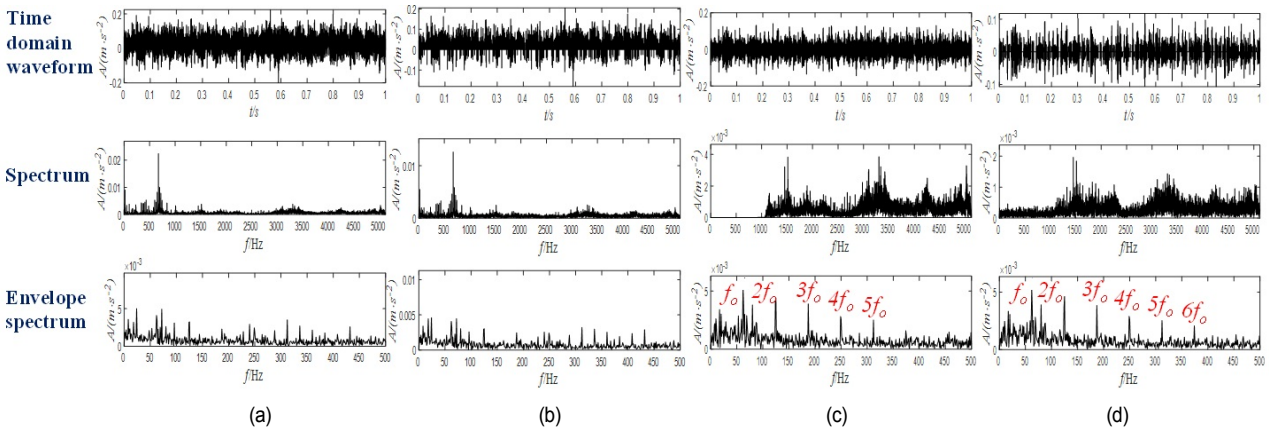

Fig. 9. Time-domain waveforms, spectra and envelope spectra: (a) raw signal; (b) without EWT decomposition; (c) denoised by the NTF; (d) denoised by the ATF.

The envelope spectra of Figs. 9(c) and (d) can effectively distinguish the fault characteristic frequency (f_o = 62 Hz). The former can distinguish the maximum frequency as the 5x frequency component, while the latter can distinguish the maximum frequency as the 6x frequency component. Furthermore, the comparison indicates that the proposed method can improve the recognition accuracy of the fault characteristic frequency and its harmonic.

Similarly, to verify the performance of the ATF, the results of the raw signal, "without EWT", the NTF, the HTF, the STF, the ITF and the ATF are compared in this section. The kurtosis, XCORR and MSE values obtained using different methods are shown in Table 4. The kurtoses of the six methods are higher than that of the raw signal. The kurtosis of the ITF is the largest, and it is slightly higher than that of the STF and ATF. Although "without EWT" and the NTF have good performance in terms of their XCORR and MSE values, their kurtosis values and improvements are minimal except in comparison with the raw signal, which is disadvantageous regarding the identification early faults and weak bearing faults. In addition, the ATF has excellent performance in terms of its XCORR and MSE values, which are better than those of the STF and ITF.

In conclusion, it is apparent from Table 4 and Fig. 9 that the individual envelope analysis approach for faulty signals is unable to identify the fault characteristic frequency. However, after decomposition with the EWT, IMFs are selected according to the given criteria, and envelope analysis is performed. Then, the fault characteristic frequency and its harmonics can be distinguished effectively. Furthermore, if the ATF is used to denoise the selected IMFs before reconstruction, the denoising effect is significantly enhanced. Moreover, the recognition accuracy of the fault frequency and its harmonic frequency in the envelope spectrum is increased, and the kurtosis is improved. Therefore, the ATF has better sensitivity to bearing outer race faults than other threshold functions. The conclusions obtained from the actual outer race fault signal analysis are consistent with the conclusions obtained from the simulation signal analysis. The results verify that the ATF is more effective than the HTF, STF and ITF.

5.1.3 Inner race fault feature extraction for REBs

Due to interference in signal acquisition and signal transmission, the obtained signal will inevitably be mixed with noise. When the inner race surface is locally damaged, the local damage position will follow the rotating shaft and rotate periodically. Additionally, the cyclic impact force of an inner race fault behaves distinctly from that of an outer race fault, and it exhibits a relevant periodic change with rotation. These factors have an adverse effect on fault feature extraction.

Fig. 11(a) shows the time-domain waveform, spectrum and envelope spectrum of the raw signal. The fault characteristic frequency is hard to accurately identify. Therefore, the proposed method is used for processing. The signal is decomposed via the EWT to obtain IMFs (Fig. 12), and the 12th, 13th, and 14th IMFs are selected. Fig. 11(b) shows the time-domain waveform, spectrum and envelope spectrum of the reconstructed signal produced without EWT decomposition. Similarly, it is difficult to extract the fault characteristic frequency in this

Table 4. Comparison of the evaluation indices produced by different methods in the actual signal analysis.

Method	Kurtosis	XCORR	MSE
The raw signal	3.1603	1	0
Without EWT	5.4375	0.8756	0.00070
No threshold function	3.9355	0.7176	0.00164
Hard threshold function	6.5246	0.5691	0.00204
Soft threshold function	14.6290	0.5015	0.00233
Improved threshold function [11]	14.6810	0.5013	0.00233
Arctangent threshold function	12.2099	0.5634	0.00211

Table 5. Comparison of the evaluation indices produced by different methods in the actual signal analysis.

Method	Kurtosis	XCORR	MSE
The raw signal	4.8596	1	0
Without EWT	9.8691	0.9039	0.00057
No threshold function	9.0890	0.3986	0.00213
Hard threshold function	33.9640	0.3064	0.00228
Soft threshold function	72.1300	0.2704	0.00236
Improved threshold function [11]	72.6500	0.2703	0.00236
Arctangent threshold function	68.2130	0.3026	0.00230

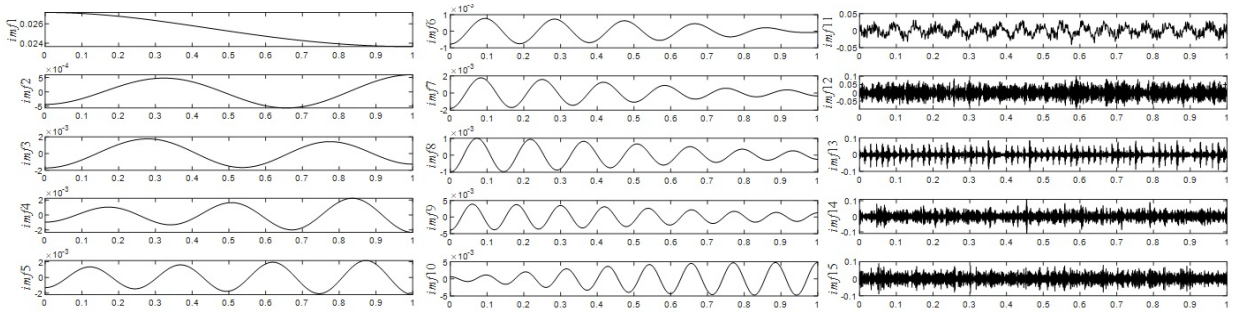

Fig. 10. Time-domain waveforms of the IMFs decomposed by the EWT.

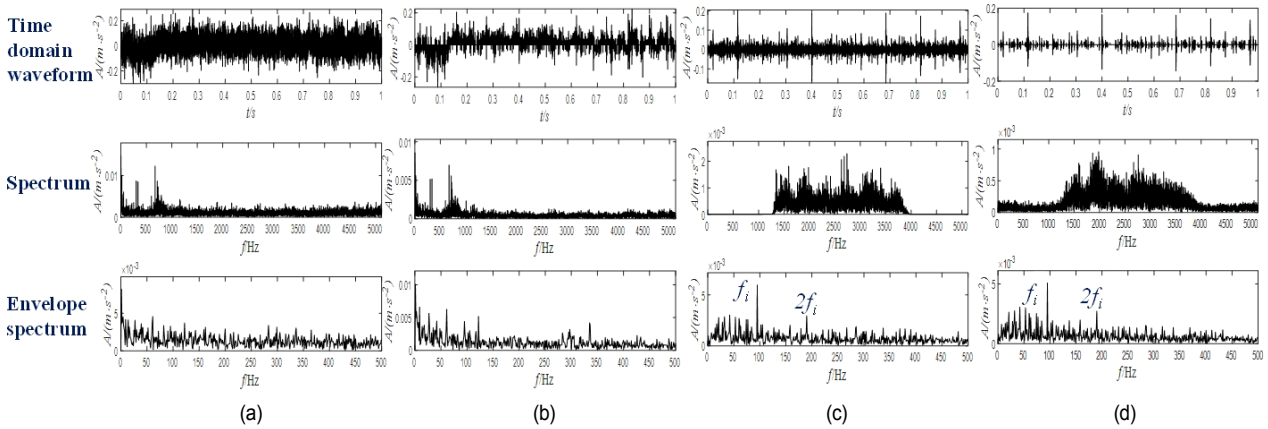

Fig. 11. Time-domain waveforms, spectra and envelope spectra: (a) raw signal; (b) without EWT decomposition; (c) denoised by the NTF; (d) denoised by the ATF.

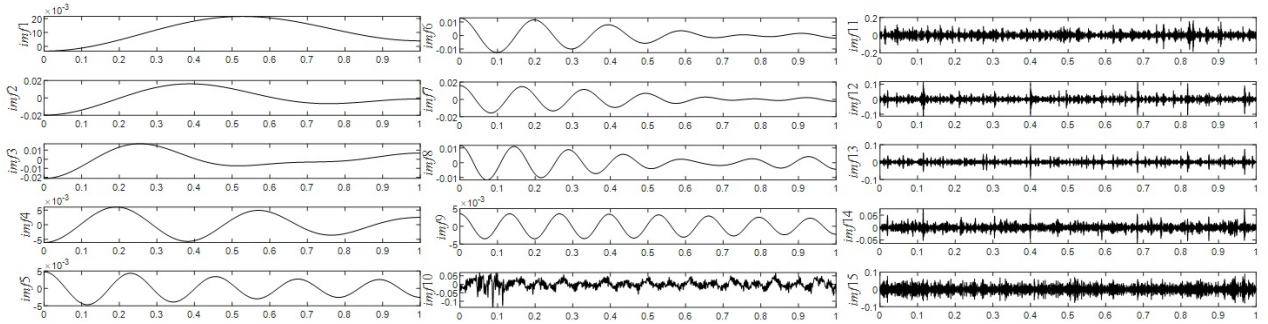

Fig. 12. Time-domain waveforms of the IMFs decomposed by the EWT.

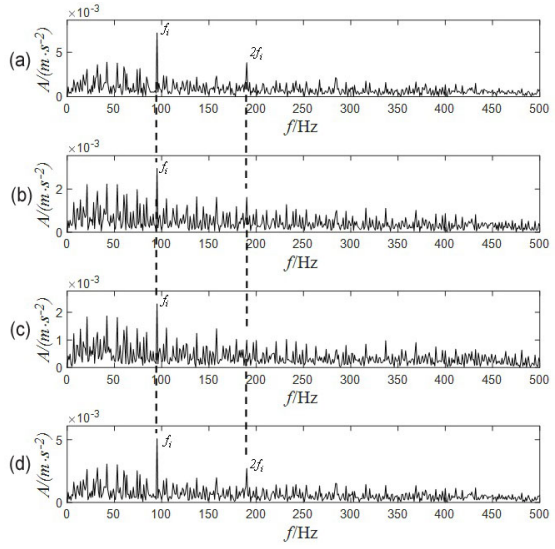

Fig. 13. The envelope spectra of the signal denoised by four threshold functions: (a) HTF; (b) STF; (c) ITF; (d) ATF.

case without EWT decomposition. From the spectrum in Fig. 11(c), it also emerges that selecting the IMF obtained by EWT decomposition is similar to bandpass filtering. From the envelope spectra of Figs. 11(c) and (d), the fault characteristic frequency (f_i = 95 Hz) can be identified, and the distinguishable maximum frequency is the 2x frequency component. However, not all threshold function methods have high recognition accuracies for the fault frequency and harmonics. Fig. 13 shows the envelope spectra of the signals denoised by the four tested threshold functions. Although all denoising methods with four different threshold functions can identify the fault characteristic frequency, it is difficult to distinguish the 2x frequency component from the envelope spectra of the STF and ITF. Therefore, the STF and ITF have worse recognition accuracy than the HTF and ATF for the fault frequency and harmonics.

Similarly, Table 5 shows the indices achieved by different methods, including their kurtosis, XCORR and MSE values. The results show that the kurtoses of the six methods are improved in comparison with that of the raw signal, and the kurtoses of the ITF and STF are very large. Although a large kurtosis is beneficial for fault identification, it also reveals that some components in the signal containing fault information are filtered. This may lead to low identification accuracy regarding the fault characteristic frequency and its harmonics. The NTF and “without EWT” have the best XCORR and MSE values, but their kurtoses exhibit only slight improvements. Furthermore, the ATF performs better than the HTF and NTF in terms of their kurtosis values, and it has the best XCORR and MSE performance, with values between those of the STF and ITF.

In summary, the experimental results obtained in the actual

Table 6. Parameters of the LDK UER204 bearings.

Parameter	Value
Outer race diameter	39.80 mm
Inner race diameter	29.30 mm
Bearing mean diameter	34.55 mm
Ball diameter	7.92 mm
Number of balls	8
Contact angle	0°
Load rating (static)	6.65 kN
Load rating (dynamic)	12.82 kN

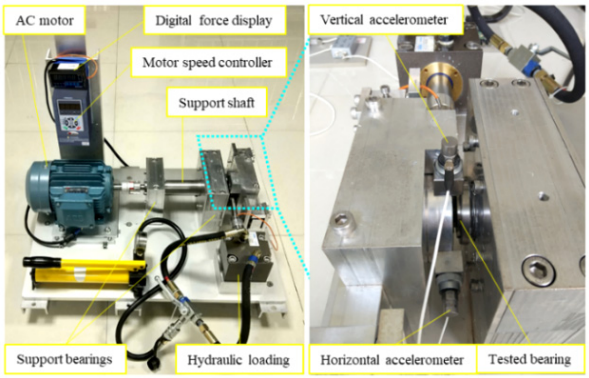

Fig. 14. The experimental bench of XJTU-SY.

faulty signal analysis of REBs verify that the ATF can effectively denoise and overcome the influence of noise in the process of bearing fault feature extraction. The ATF is better than the HTF, STF and ITF. Consequently, the proposed method is appropriate for denoising, and it has practical value in fault feature extraction for REBs.

5.2 Case 2: open-source XJTU-SY dataset

5.2.1 Data sources and data description

To further verify the superior denoising and fault feature extraction performance of the proposed method, the open-source XJTU-SY REB dataset provided by Xi'an Jiaotong University (XJTU) and Changxing Sumyoung Technology Co., Ltd. (SY) is selected in this section [28, 29]. As shown in Fig. 14, the experimental bench is composed of an alternating current (AC) induction motor, a motor speed controller, a support shaft, two support bearings (heavy duty roller bearings), a hydraulic loading system and so on. The tested bearings are LDK UER204 bearings, and their detailed parameters are given in Table 6. The XJTU-SY bearing dataset contains the run-to-failure vibration signals of 15 REBs under three different operating conditions, as shown in Table 7. In the experiment, the sampling frequency is set to 25.6 kHz, 32768 sampling points are used for each sampling, and the sampling period is 1 min. In this section, the outer race fault data of *bearing 3-1* and inner ring fault data of *bearing 3-3* under the third working condition are selected as the analysis data. According to Eqs. (31) and (32),

Table 7. XJTU-SY bearing dataset.

Operating condition	Bearing dataset	Bearing lifetimes	Fault type
1 (35 Hz/ 12 kN)	Bearing 1_1	2 h 3 min	Outer race
	Bearing 1_2	2 h 41 min	Outer race
	Bearing 1_3	2 h 38 min	Outer race
	Bearing 1_4	2 h 2 min	Cage
	Bearing 1_5	52 min	Inner race & outer race
2 (37.5 Hz/ 11 kN)	Bearing 2_1	8 h 11 min	Inner race
	Bearing 2_2	2 h 41 min	Outer race
	Bearing 2_3	8 h 53 min	Cage
	Bearing 2_4	42 min	Outer race
	Bearing 2_5	5 h 39 min	Outer race
3 (40 Hz/ 10 kN)	Bearing 3_1	42 h 18 min	Outer race
	Bearing 3_2	41 h 36 min	Inner race, outer race, ball & cage
	Bearing 3_3	6 h 11 min	Inner race
	Bearing 3_4	25 h 15 min	Inner race
	Bearing 3_5	1 h 54 min	Outer race

it is calculated that the outer ring fault frequency is approximately 123 Hz, and the inner ring fault frequency is approximately 197 Hz.

5.2.2 Outer race fault feature extraction for REBs

Fig. 15(a) shows the time-domain waveform, frequency spectrum and envelope spectrum of the signal. Fig. 16 shows the IMFs obtained after EWT decomposition. The 1st, 3rd, 4th and 5th IMFs are selected. Fig. 15(b) shows the time-domain waveform, spectrum and envelope spectrum of the signal produced without EWT decomposition. As shown in Figs. 15(a) and (b), the fault characteristic frequency cannot be directly extracted from these IMFs. Fig. 15(c) shows the time-domain waveform, frequency spectrum and envelope spectrum of the reconstructed signal obtained with NTF denoising. Fig. 15(d) shows the time-domain waveform, frequency spectrum and envelope spectrum of the reconstructed signal denoised by the ATF. From the envelope spectra of Figs. 15(c) and (d), the fault characteristic frequency (f_o = 123 Hz) can be identified, and the distinguishable maximum frequency is the 4x frequency component.

Similar to the previous case, the same comparative experiment is used here. It can be seen from Fig. 15 and Table 8 that the proposed method enhances the recognition accuracy of the fault frequency and its harmonic frequency in the envelope spectrum. The results verify that the ATF is more effective than the HTF, STF and ITF.

5.2.3 Inner race fault feature extraction for REBs

Additionally, an inner race fault signal is processed. Fig. 17(a) shows the time-domain waveform, frequency spectrum and

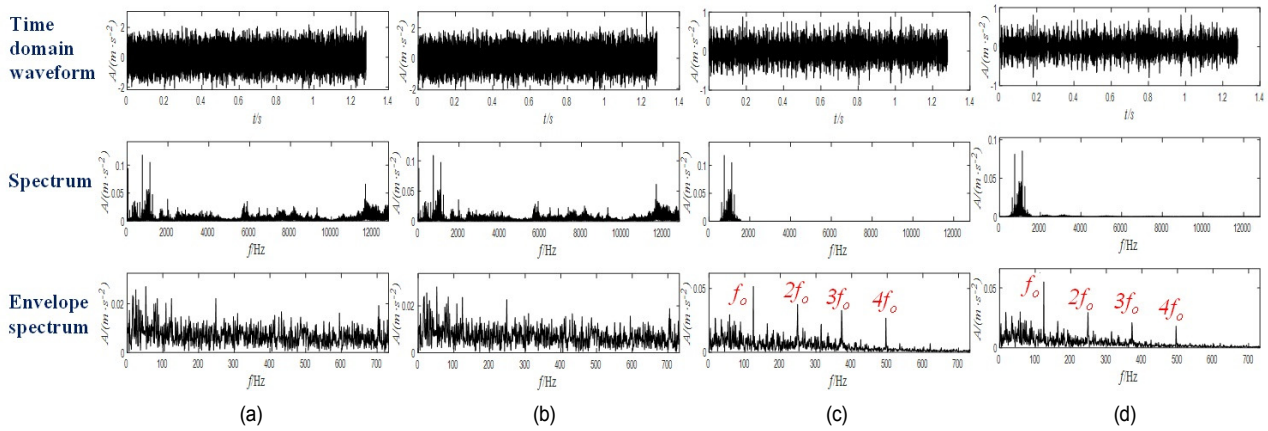

Fig. 15. Time-domain waveforms, spectra and envelope spectra: (a) raw signal; (b) without EWT decomposition; (c) denoised by the NTF; (d) denoised by the ATF.

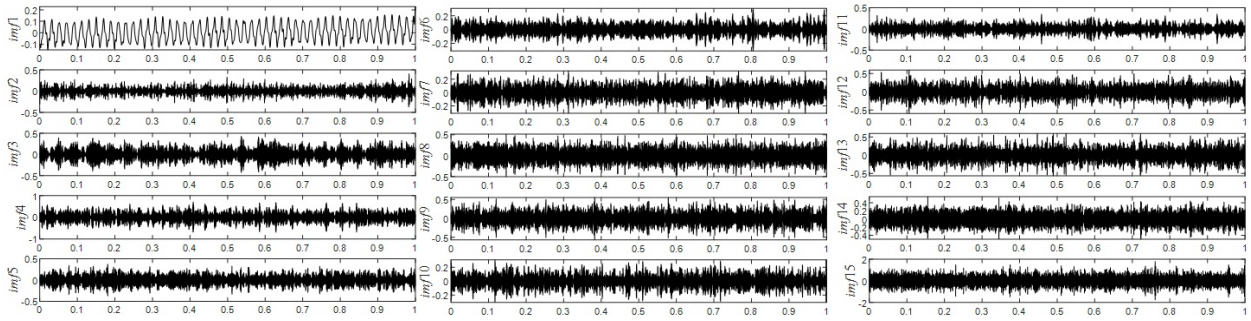

Fig. 16. Time-domain waveforms of the IMFs decomposed by the EWT.

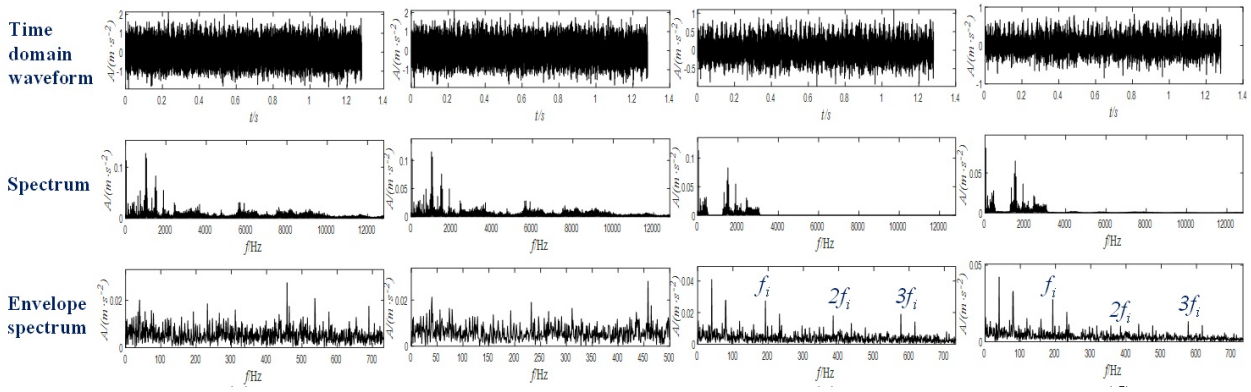

Fig. 17. Time-domain waveforms, spectra and envelope spectra: (a) raw signal; (b) without EWT decomposition; (c) denoised by the NTF; (d) denoised by the ATF.

envelope spectrum of the signal. Fig. 18 shows the IMFs produced after EWT decomposition. Fig. 17(b) shows the time-domain waveform, spectrum and envelope spectrum of the signal produced without EWT decomposition. Neither Figs. 17(a) nor (b) can be used to accurately determine the fault characteristic frequency. The 3rd and 4th IMFs are selected. The reconstructed signal is denoised by the NTF and ATF, and the results are shown in Figs. 17(c) and (d), respectively. The rotational frequency (40 Hz) and the fault characteristic frequency (f_i = 197 Hz) can be identified, and the distinguishable maximum frequency is the 3x frequency component. Table 9 shows the evaluation indicators yielded by the different methods. Fig. 19 shows the envelope spectra of the four threshold functions. Through the analysis conducted on the XJTU-SY dataset, it can be concluded that the proposed method enhances the recognition accuracy of the fault frequency and its harmonic frequency in the envelope spectrum. In addition, the ATF has better performance than the HTF, STF and ITF.

Table 8. Comparison of the evaluation indices produced by different methods in the actual signal analysis.

Method	Kurtosis	XCORR	MSE
The raw signal	3.0915	1	0
Without EWT	3.6002	0.9925	0.00671
No threshold function	2.9840	0.4008	0.28062
Hard threshold function	3.6165	0.3686	0.28491
Soft threshold function	7.4325	0.3376	0.30542
Improved threshold function [11]	8.2587	0.3338	0.30421
Arctangent threshold function	6.7230	0.3685	0.28494

Table 9. Comparison of the evaluation indices produced by different methods in the actual signal analysis.

Method	Kurtosis	XCORR	MSE
The raw signal	3.0139	1	0
Without EWT	3.0837	0.9923	0.00498
No threshold function	3.0469	0.5147	0.17493
Hard threshold function	3.1736	0.4996	0.17858
Soft threshold function	4.2780	0.4755	0.19181
Improved threshold function [11]	4.4200	0.4736	0.19103
Arctangent threshold function	4.2270	0.4958	0.18147

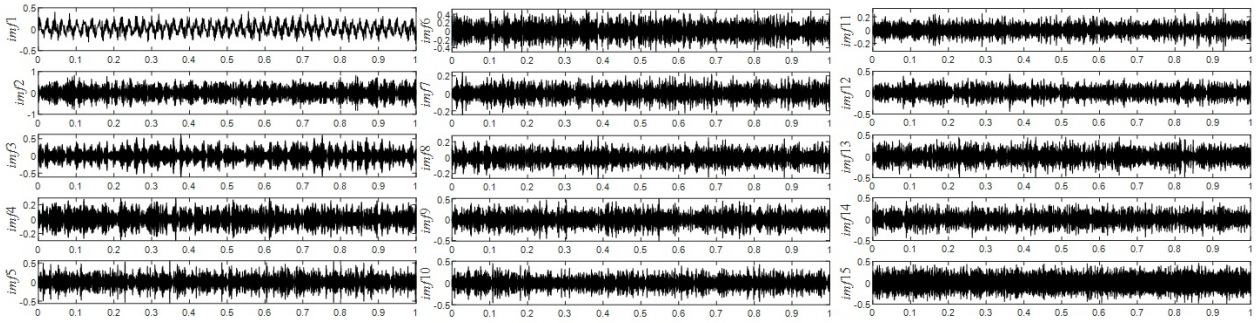

Fig. 18. Time-domain waveforms of the IMFs decomposed by the EWT.

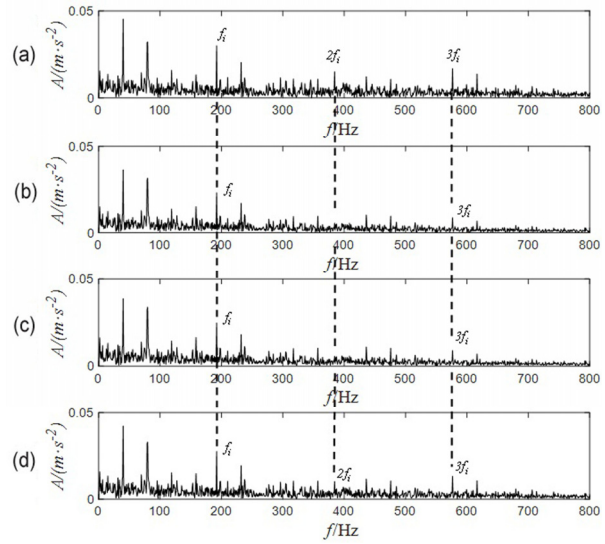

Fig. 19. The envelope spectra of the signal denoised by four threshold functions: (a) HTF; (b) STF; (c) ITF; (d) ATF.

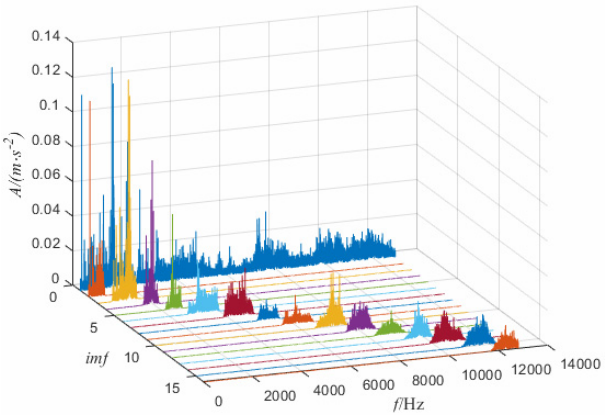

Fig. 20. 3D image of the IMFs spectra.

6. Discussions

6.1 Antinoise performance of the proposed method

From the previous analysis, it is known that the proposed method is effective in REB fault feature extraction and enhances the recognition accuracy of the fault characteristic frequency and its harmonics. The process of utilizing EWT decomposition to obtain IMFs acts as a filtering approach that employs multiple bandpass filters (Fig. 20). IMFs are obtained by segmenting the spectrum of the raw input signal, and each IMF revolves around a specific frequency, which makes it possible to achieve the desired denoising effect by selecting IMFs that are more impactful. In particular, the whole process is data-driven and adaptive.

The good denoising performance of the ATF has also been verified through several comparative experiments, although the antinoise limit of the ATF and the proposed method is not clear. Therefore, based on the simulation model established in Sec. 4.1, this section tests the antinoise performance of the proposed method by processing signals with different SNRs [-5 dB, -10 dB, -12 dB, -15 dB, -20 dB]. Fig. 21 shows the obtained results, with the first row showing the time-domain waveforms,

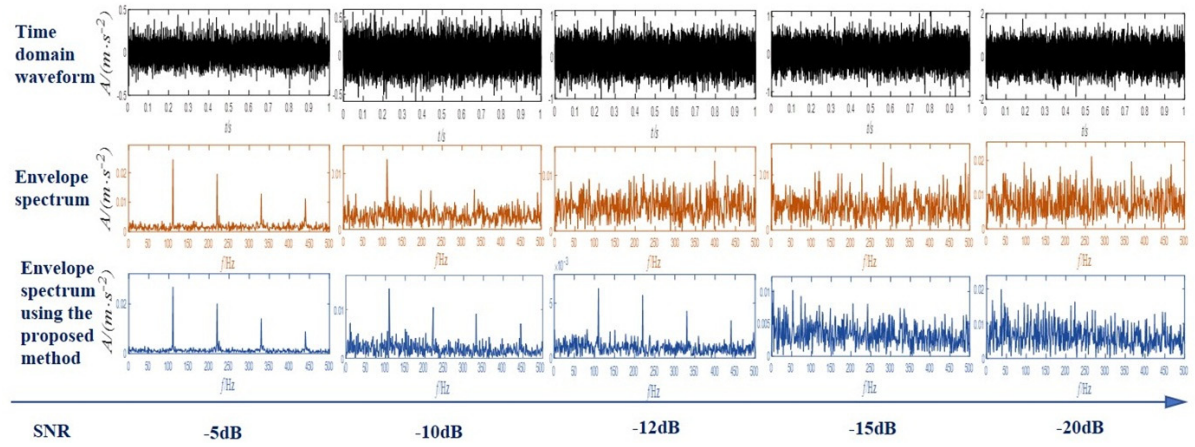

Fig. 21. The results obtained under different SNRs.

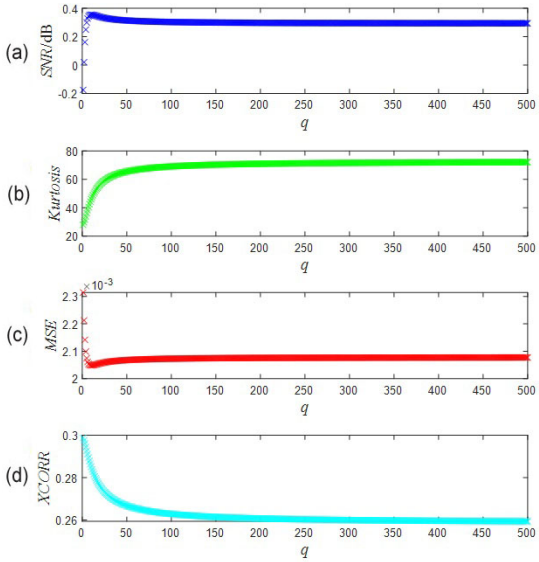

Fig. 22. Scatter diagrams: (a) SNR; (b) kurtosis; (c) MSE; (d) XCORR.

the second row showing the envelope spectra obtained with a direct envelope analysis, and the third row showing the envelope spectra processed by the proposed method; different SNRs are presented in the horizontal coordinates. It can be seen from Fig. 21 that when the SNR is -5 dB, both methods can effectively extract the fault characteristic frequency and its harmonics; when the SNR is -10 dB, both methods can extract the fault characteristic frequency, but the harmonics in the envelope spectrum obtained with the single envelope analysis become inconspicuous due to the interference of noise; when the SNR is -12 dB, only the proposed method can effectively extract the fault characteristic frequency; and when the SNR is -15 dB or -20 dB, neither method can accurately extract the fault characteristic frequency.

6.2 Analysis of the position parameter q

The ATF is proposed in Sec. 2.3, and an important position parameter q is mentioned in the same section. The value of q directly affects the hard or soft characteristics of the ATF and thus affects the denoising performance and the accuracy of fault feature extraction.

Based on the outer ring fault simulation model proposed in Sec. 4.1, the value of q ranges from λ to 500 λ (the step size is λ), and scatter diagrams of the SNR, kurtosis, MSE and XCORR metrics are drawn. As shown in Fig. 22, the SNR increases first and then decreases as q increases, and the SNR reaches its maximum when q equals 10 λ; the kurtosis increases as q increases; the MSE decreases and then increases as q increases; and the XCORR decreases as q increases.

Although the selection of the q parameter is investigated via traversal, this does not mean that the same q can be used in all cases. The evaluation indicators have different features when processing other bearing fault data. In practice, the value of the position parameter q can be adjusted according to the feedback derived from the obtained results.

7. Conclusions

An REB fault feature extraction method based on the EWT and an ATF is proposed. Aiming at the discontinuity of the HTF at the threshold and the constant deviation of the STF, the ATF is established, which can change “hard” or “soft” characteristics by adjusting the position parameter. To verify the performance of the ATF, the HTF, the STF, the ITF in Ref. [11] and several methods are compared in terms of denoising simulation signals and actual fault signals (including two cases). Four indicators, the kurtosis, SNR, XCORR and MSE metrics, are adopted to evaluate their superiority. Eventually, the experimental results reveal that the ATF has a powerful denoising ability, and the proposed method can achieve high recognition accuracy regarding the fault characteristic frequency and its harmonics.

In the future, we will concentrate on the weak fault feature extraction ability of the proposed method under a strong noise background. Considering the importance of the threshold value

in threshold denoising and the parameter selection process in the ATF, the study of efficient threshold estimation methods and parameter selection approaches through adaptive optimization algorithms will become the focus of subsequent research.

Acknowledgments

This work was supported by the National Natural Science Foundation of China (51975117), and Jiangsu Provincial Key Research and Development Program (BE2019086).

References

[1] L. Ciabattoni et al., Statistical spectral analysis for fault diagnosis of rotating machines, *IEEE Trans. Ind. Electron.*, 65 (5) (2018) 4301-4310.

[2] H.-T. Yau et al., Fractional-order chaotic self-synchronization-based tracking faults diagnosis of ball bearing systems, *IEEE Trans. Ind. Electron.*, 63 (6) (2016) 3824-3833.

[3] C. Sun et al., Support vector machine-based Grassmann manifold distance for health monitoring of viscoelastic sandwich structure with material ageing, *J. Sound Vib.*, 368 (2016) 249-263.

[4] W. Qiao and D. Lu, A survey on wind turbine condition monitoring and fault diagnosis-part ii: signals and signal processing methods, *IEEE Trans. Ind. Electron.*, 62 (10) (2015) 6546-6557.

[5] A. Wan et al., Prognostics of gas turbine: a condition-based maintenance approach based on multi-environmental time similarity, *Mech. Syst. Signal Process.*, 109 (2018) 150-165.

[6] B. Cai et al., A data-driven fault diagnosis methodology in three-phase inverters for PMSM drive systems, *IEEE Trans. Power Electron.*, 32 (7) (2017) 5590-5600.

[7] D. L. Donoho, De-noising by soft-thresholding, *IEEE Trans. Inf. Theory*, 41 (3) (1995) 613-627.

[8] D. L. Donoho and I. M. Johnstone, Adapting to unknown smoothness via wavelet shrinkage, *J. Am. Stat. Assoc.*, 90 (432) (1995) 1200-1224.

[9] Z. Meng and S. Li, Rolling bearing fault diagnosis based on improved wavelet threshold de-noising method and HHT, *J. Vib. Eng.*, 32 (14) (2013) 204-208+214.

[10] B. Xie et al., Gamma spectrum denoising method based on improved wavelet threshold, *Nucl. Eng. Technol.*, 52 (8) (2020) 1771-1776.

[11] J. Li et al., Downhole microseismic signal denoising via empirical wavelet transform and adaptive thresholding, *J. Geophys. Eng.*, 15 (6) (2018) 2469-2480.

[12] S. N. Chegini, A. Bagheri and F. Najafi, Application of a new EWT-based denoising technique in bearing fault diagnosis, *Measurement*, 144 (2019) 275-297.

[13] W. Chen et al., Fault feature extraction and diagnosis of rolling bearings based on wavelet thresholding denoising with CEEMDAN energy entropy and PSO-LSSVM, *Measurement*, 172 (2021) 108901.

[14] F. He et al., Blind denoising of 3D seismic signals based on the wave atom transform, *J. Vib. Shock*, 38 (8) (2019) 88-95.

[15] P. Chen and Q. Zhang, Classification of heart sounds using discrete time-frequency energy feature based on S transform and the wavelet threshold denoising, *Biomed. Signal Process. Control*, 57 (2020) 101684.

[16] P. Wang et al., Bearing fault signal denoising method of hierarchical adaptive wavelet threshold function, *J. Vib. Eng.*, 32 (3) (2019) 548-556.

[17] H. Liu et al., A de-noising method using the improved wavelet threshold function based on noise variance estimation, *Mech. Syst. Signal Process.*, 99 (2018) 30-46.

[18] F. M. Bayer, A. J. Kozakevicius and R. J. Cintra, An iterative wavelet threshold for signal denoising, *Signal Processing*, 162 (2019) 10-20.

[19] D. L. Donoho and I. M. Johnstone, Ideal spatial adaptation by wavelet shrinkage, *Biometrika*, 81 (3) (1994) 425-455.

[20] S. G. Chang, B. Yu and M. Vetterli, Adaptive wavelet thresholding for image denoising and compression, *IEEE Trans. Image Process.*, 9 (9) (2000) 1532-1546.

[21] S. Poornachandra, Wavelet-based denoising using subband dependent threshold for ECG signals, *Digit. Signal Process. A Rev. J.*, 18 (1) (2008) 49-55.

[22] J. Gilles, Empirical wavelet transform, *IEEE Trans. Signal Process.*, 61 (16) (2013) 3999-4010.

[23] N. E. Huang et al., A confidence limit for the empirical mode decomposition and Hilbert spectral analysis, *Proc. R. Soc. London. Ser. A Math. Phys. Eng. Sci.*, 459 (2037) (2003) 2317-2345.

[24] X. Yan and M. Jia, Application of CSA-VMD and optimal scale morphological slice bispectrum in enhancing outer race fault detection of rolling element bearings, *Mech. Syst. Signal Process.*, 122 (2019) 56-86.

[25] Y. Miao et al., Application of an improved maximum correlated kurtosis deconvolution method for fault diagnosis of rolling element bearings, *Mech. Syst. Signal Process.*, 92 (2017) 173-195.

[26] M. S. Sadooghi and S. Esmaeilzadeh Khadem, A new performance evaluation scheme for jet engine vibration signal denoising, *Mech. Syst. Signal Process.*, 76-77 (2016) 201-212.

[27] R. Abdelkader, A. Kaddour and Z. Derouiche, Enhancement of rolling bearing fault diagnosis based on improvement of empirical mode decomposition denoising method, *Int. J. Adv. Manuf. Technol.*, 97 (5-8) (2018) 3099-3117.

[28] B. Wang, *XJTU-SY Bearing Datasets*, http://biaowang.tech/xjtu-sy-bearing-datasets/.

[29] B. Wang et al., A hybrid prognostics approach for estimating remaining useful life of rolling element bearings, *IEEE Transactions on Reliability*, 69 (1) (2018) 401-412.

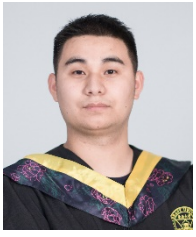

Chao Li received the B.S. degree in Mechanical Engineering from Southeast University, Nanjing, China, in 2020. He is currently pursuing M.S. degree from Southeast University, Nanjing, China. His main research interests include signal processing and fault diagnosis.

Feiyun Xu received the Ph.D. degree in Precision Instrumentation and Machinery from Southeast University, Nanjing, China, in 1996. Currently, he is a Professor of Mechanical Engineering, Southeast University, China. His main research interests include artificial intelligence theory and application, measurement and control technology, time series analysis and nonlinear system identification.

Hongxin Yang received the B.S. degree in Mechanical Engineering from Chongqing University, Chongqing, China, in 2020. He is currently pursuing M.S. degree from Southeast University, Nanjing, China. His main research interests include signal processing, FPGA and fault diagnosis.

Lei Zou received the M.S. degree in Mechanical Engineering from Southeast University, Nanjing, China, in 2021. His main research interests include signal processing, electromechanical equipment intelligent monitoring and fault diagnosis.